energies

MDPI

Article

Developing an Automated Tool for Quantitative Analysis of the Deconvoluted Electrochemical Impedance Response of a Solid Oxide Fuel Cell

Mohammad Alboghobeish [1,2], Andrea Monforti Ferrario [1,3], Davide Pumiglia [1], Massimiliano Della Pietra [1], Stephen J. McPhail [1,*], Sergii Pylypko [4] and Domenico Borello [5]

[1] ENEA Department of Energy Technologies and Renewable Sources, Energy Storage, Batteries and Hydrogen Production & Use (TERIN-PSU-ABI), Via Anguillarese, 00123 Rome, Italy; mohammad.alboghobeish001@studenti.uniparthenope.it (M.A.); andrea.monfortiferrario@enea.it (A.M.F.); davide.pumiglia@enea.it (D.P.); massimiliano.dellapietra@enea.it (M.D.P.)

[2] Dipartimento di Ingegneria, Università degli Studi di Napoli Parthenope, Centro Direzionale Isola C4, 80143 Napoli, Italy

[3] Department of Industrial Engineering and Mathematical Sciences, Università Politecnica delle Marche, Via Brecce Bianche, 60131 Ancona, Italy

[4] Elcogen AS, Valukoja 23, 11415 Tallinn, Estonia; sergii.pylypko@elcogen.com

[5] Dipartimento di Ingegneria Meccanica e Aerospaziale (DIMA), Sapienza University of Rome, Via Eudossiana, 18, 00184 Roma, Italy; domenico.borello@uniroma1.it

* Correspondence: stephen.mcphail@enea.it

Abstract: Despite being commercially available, solid oxide fuel cell (SOFC) technology requires further study to understand its physicochemical processes for diagnostics, prognostics, and quality assurance purposes. Electrochemical impedance spectroscopy (EIS), a widely used characterization technique for SOFCs, is often accompanied by the distribution of relaxation times (DRT) as a method for deconvoluting the contribution of each physicochemical process from the aggregated impedance response spectra. While EIS yields valuable information for the operation of SOFCs, the quantitative analysis of the DRT and its shifts remains cumbersome. To address this issue, and to create a replicable benchmark for the assessment of DRT results, a custom tool was developed in MATLAB to numerically analyze the DRT spectra, identify the DRT peaks, and assess their deviation in terms of peak frequency and DRT amplitude from nominal operating conditions. The preliminary validation of the tool was carried out by applying the tool to an extensive experimental campaign on 23 SOFC button-sized samples from three production batches in which EIS measurements were performed in parametric operating conditions. It was concluded that the results of the automated analysis via the developed tool were in accordance with the qualitative analysis of previous studies. It is capable of providing adequate additional quantitative results in terms of DRT shifts for further analysis and provides the basis for better interoperability of DRT analyses between laboratories.

Keywords: solid oxide fuel cell; physicochemical processes; electrochemical impedance spectroscopy; distribution of relaxation times; MATLAB tool; electrochemical characterization

check for updates

Citation: Alboghobeish, M.; Monforti Ferrario, A.; Pumiglia, D.; Della Pietra, M.; McPhail, S.J.; Pylypko, S.; Borello, D. Developing an Automated Tool for Quantitative Analysis of the Deconvoluted Electrochemical Impedance Response of a Solid Oxide Fuel Cell. *Energies* **2022**, *15*, 3702. https://doi.org/10.3390/en15103702

Academic Editor: Mario Aparicio

Received: 25 March 2022
Accepted: 3 May 2022
Published: 18 May 2022

Publisher's Note: MDPI stays neutral with regard to jurisdictional claims in published maps and institutional affiliations.

Copyright: © 2022 by the authors. Licensee MDPI, Basel, Switzerland. This article is an open access article distributed under the terms and conditions of the Creative Commons Attribution (CC BY) license (https://creativecommons.org/licenses/by/4.0/).

1. Introduction

Solid oxide fuel cells (SOFCs) are categorized as high-temperature fuel cells since they operate at an elevated temperature range (600–900 °C). This range of temperature brings significant advantages in terms of applications [1,2]. It allows for favorable thermodynamic conditions and improved reaction kinetics, leading to high overall conversion efficiencies [3]. In addition, it allows for the processing of a variety of carbonaceous fuels [4] and the use of less costly electrocatalysts, which has brought renewed attention to the technology for cost-containment reasons [5]. Finally, the adsorption of various gas species to the surface of

electrodes (e.g., the poisoning effect of CO related to low-temperature fuel cells) is mitigated in SOFCs [6,7].

SOFCs are anticipated to play a significant role in polygenertion applications such as combined cooling, heating, and power (CCHP) systems thanks to their fuel flexibility and high conversion efficiency besides their low level of emissions [8]. SOFCs can be fed with both pure hydrogen as well as natural gas, representing a suitable and flexible candidate for stationary power generation. Redirecting the exhaust gases into heat recovery units required for heating and refrigeration [9] allows us to achieve exceptionally high overall (electrical + thermal) conversion efficiencies of over 90%. Recent studies focus on feeding the SOFCs with renewable fuels such as green hydrogen, biogas, syngas, and other synthetic fuels and derivatives and addressing system performance in different configurations and operating conditions and under durability challenges [10].

A SOFC is made of an electrolyte between a positive electrode, the cathode, and a negative electrode, the anode [11]. At temperatures higher than 500 °C, the electrolyte becomes a conductor for O^{2-} ions originating in the cathode (oxygen electrode), where O_2 is dissociated [12]. Once the O^{2-} ions cross the electrolyte, they are recombined with H_2 directly or indirectly provided to the anode (fuel electrode), forming water and releasing electrons [13].

Electrochemical impedance spectroscopy (EIS) is a robust method for the electrochemical characterization of a SOFC. It provides insight into different overpotentials in an electrochemical device as a function of the process's frequency or characteristic time [14]. In order to perform an EIS measurement, a sinusoidal alternating current or voltage signal is applied to the tested sample at varying frequencies [15]. The sample's impedance will then be measured using the input and response signals. The acquired impedance can be viewed in a Nyquist (display of the real and imaginary components of the impedance) or a Bode plot (plot of the real and imaginary parts of the impedance against frequency) [16]. Guidelines on the carrying out and interpretation of EIS measurement on SOC cell/stack assemblies are provided in IEC Standard 62282-8-101.

EIS data show the convoluted impedance response of the SOFC sample. The distribution of relaxation times (DRT) approach is a widely used electrochemical impedance analysis method for separating the impedance response into discrete components linked to each physicochemical process occurring within the cell [17,18]. Calculating the DRT may lead to a practical approach to describing the deconvoluted physicochemical behavior of SOFCs [19,20].

The DRT permits the accurate detection of each of the processes that produce the impedance spectra of SOFCs during fuel cell characterization [21]. Therefore, physically significant information can be obtained [22]. Furthermore, the DRT enables the accurate distinction of each polarization process's characteristic frequencies and qualitative analysis of the extent of its effect on the overall polarization spectra [23], see Figure 1. By comparing DRT spectra obtained with the same experimental procedures of the SOFC sample under different experimental conditions (e.g., variation of temperatures or reactant compositions), it is possible to ascertain the latter's influence on SOFC processes by analyzing the shifts in the DRT peaks and their characteristic frequency bandwidths [24,25]. However, DRT shifts are often analyzed only qualitatively by visual inspection since a quantitative analysis is cumbersome [26,27].

A variety of codes have been developed by different research groups to calculate the DRT spectra of EIS data. A well-known one is DRTtools [28], which studies the effect of discretization methods on the DRT. Risse et al. introduced the DRT-LMA [29], which utilizes an iterative method, the Levenberg–Marquardt algorithm (LMA), to calculate the relaxation times function. Li et al. [17] proposed a procedure that automatically estimates the regularization parameter of the Ridge and Lasso methods based on information criteria. The work of Žic et al., DFRT-Py, discusses a multi-parameter regularization approach to address the issues of high data corruption in experimental EIS data analysis [30]. Kulikovsky [31] reported a method for DRT calculation that combines Tikhonov regularization and the

projected gradient method, called TRPG, for increased simplicity and speed. Kobayashi et al. [32] attempted to generalize the DRT analysis by introducing an iterative elastic net regularization algorithm based on LMA.

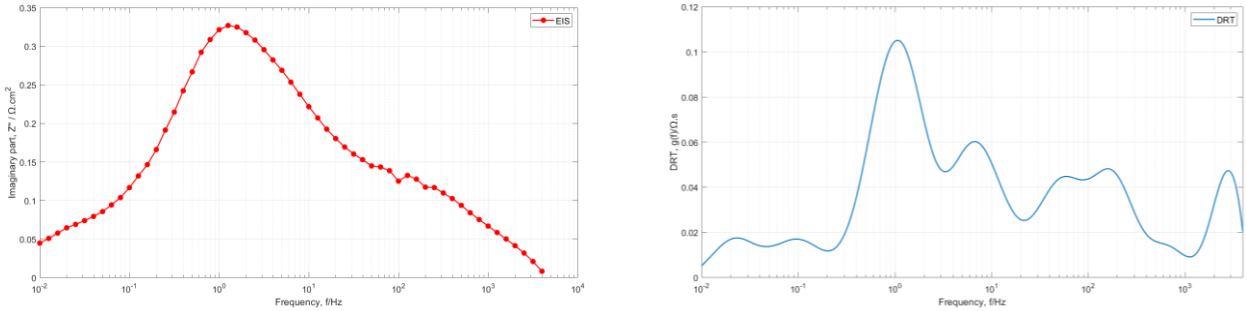

(**a**) (**b**)

Figure 1. Comparison of the (**a**) EIS measurement and (**b**) its DRT deconvolution of one of the samples analyzed in this study.

The input DRT data used in this work were obtained from an in-house developed code at ENEA Casaccia Research Center that has been used and validated in previously published studies [33,34]. In this work, the main goal was to develop an automated DRT data analysis tool to identify and assess the DRT peak shifts—both in amplitude and frequency—with variating operating conditions. The proposed tool provides quantitative information regarding the trends of each impedance contribution, facilitating correct process identification and interpretation during SOFC characterization. The tool is applied to a wide range of experimental data obtained from extensive button cell testing (3 cell batches with 23 total SOFC button cell samples tested) in order to preliminarily validate the concept.

The main element of novelty of the developed tools consists of the quantitative analysis of the DRT data itself, providing an additional instrument for more precise and repeatable DRT spectra interpretation. This goes beyond the scope of the reviewed DRT methods, which mainly focus on the conversion of EIS data to DRT functions, without a quantitative and comparative analysis of the obtained DRT spectra.

2. Materials and Methods

This section covers the technical aspects of the experiments carried out on the SOFC samples (Section 2.1), addresses the properties of the tested samples, gives an overview of the used test setup and experimental procedures, and then describes the automated tool principles and development features (Section 2.2).

2.1. Experimental Analysis

The experimental investigation of button cell samples is presented to identify the physicochemical processes driving the operation of intermediate temperature SOFCs. The DRT method was performed on the experimental EIS spectra obtained from several button cell samples to achieve this result. From the systematic variation of a single operating parameter at a time, the observed response of DRT peaks could be ascribed to different electrochemical processes occurring at the anode or the cathode side, such as charge transfer and mass transport mechanisms. The experimental campaign carried out on button cell samples has a general validity for the physicochemical processes occurring in the bulk of the cells. The reduced dimensions of this kind of sample allow us to neglect the impact of concentration and temperature gradients arising on a SOFC sample of realistic size.

With the aim of assigning each peak defined by DRT functions to a single physicochemical process that governs the operation of a SOFC, the fuel cell samples were operated while varying only one operating parameter at a time: temperature, anode hydrogen content, and

cathode oxygen content. An EIS measurement was taken for each condition, and the DRT function was elaborated for each impedance measurement. In this way, it was possible to isolate the effect on the DRT peaks of each value of an analyzed operating parameter to ultimately obtain a reliable process map in terms of frequency ranges and amplitude.

2.1.1. Test Samples

Anode-supported planar intermediate temperature SOFCs manufactured and provided by Elcogen (Tallinn, Estonia) were used in this work. The cells were composed of a thin (c.a. 3 µm) dense YSZ (8% yttria-stabilized zirconia) electrolyte layer, a porous Ni-YSZ anode layer (c.a. 400 µm)—divided in a thin anode contact (c.a. 5–10 µm), a thick anode substrate and a thin functional layer (c.a. 12 µm)—a GDC (gadolinia doped ceria) diffusion barrier layer (c.a. 5 µm), and an LSC (lanthanum-strontium-cobaltite) cathode layer (c.a. 15 µm). Table 1 summarizes the constituent materials and geometry of the layers. The anode substrate was made by tape casting of NiO-YSZ suspensions; the other half-cell layer together with the electrolyte layer were deposited on this substrate by tape casting a dense YSZ suspension and sintered to form a dense film. The GDC diffusion barrier and the LSC cathode layer were applied following screen printing and sintering. As illustrated in Figure 2 below, the tested cells are button-sized with an active area of 2 cm^2.

Table 1. The materials and thicknesses of all the layers of button cells.

	Material	Thickness		Operating Temperature
Anode	Ni-YSZ	400 µm (total)	12 µm contact layer 375–385 µm support layer 12 µm active layer	650–700 °C
Electrolyte	YSZ		3 µm	
Barrier layer	GDC		5 µm	
Cathode	LSC		15 µm	

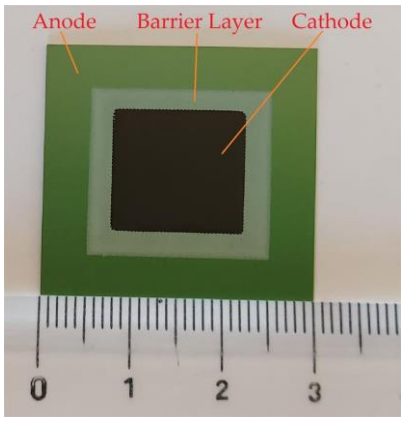

Figure 2. SOFC button cell sample.

Three different production batches (Batch 1, 7 cells; Batch 2, 11 cells; Batch 3, 5 cells; for a total of 23 cells) of the same cell design were tested. While Batch 1 and Batch 2 are identical, Batch 3 was produced with a slight modification in the manufacturing process, resulting in a denser anode functional layer, as discussed in detail in [25].

A temperature-controlled furnace forms the button cell test apparatus. A SOFC button cell sample is contained in a dual atmosphere alumina cylindrical housing, which is then attached with a high-temperature ceramic paste that retains gas tightening after thermal hardening according to manufacturer recommendations. The cell is positioned vertically, with two current collectors in contact with the sample's two electrodes, one constructed of nickel netting for the anode surface and the other of gold mesh for the cathode surface. The cell is fed with hydrogen at the anode and air that is either enriched

or depleted in oxygen content at the cathode thanks to a system of mass flow controllers (MFCs). The test bench incorporates an Agilent E3634A direct current supply, which also serves as an electronic load, an Agilent 34970A data logger, and LABVIEW-based controller software. For electrochemical impedance spectroscopy measurements, the setup was equipped with a Solartron 1260 frequency response analyzer module and a coupled Solartron 1287 Electrochemical Interface. More details regarding the test rig can be found in [25].

2.1.2. Start-Up Procedure

The button cell samples were heated to 700 °C by a temperature ramp of 0.5 °C/min with 50 mL/min N_2 to the anode and 100 mL/min air to the cathode. Hydrogen was gradually increased at the anode up to a 150 mL/min flow rate, and N_2 flow was gradually reduced. The airflow was then increased to 250 mL/min to the cathode. The cells were then left at these conditions for 1 h for stabilization. IV curves and EIS measurements were performed at 700 °C in OCV conditions and under an anode gas feed of 75 mL/min hydrogen and 75 mL/min N_2 (50/50% H_2/N_2 composition) and a cathode air feed (21% O_2) of 250 mL/min, referred to as standard conditions (StdCond) to describe the performance and impedance response of the test specimens. The characterization was carried out before and after a stabilization procedure of at least 50 h at 700 °C and 0.5 A/cm^2 to ensure stationary conditions of the measured quantities. The EIS spectrum was measured in standard conditions at OCV between 100 kHz and 10 mHz with a 10 mV amplitude. The polarization curves were performed from the OCV state to the maximum current value at which the cell voltage was above 700 mV, increasing the current at 50 mA/min steps.

2.1.3. Parameter Variations

As discussed above, to identify the processes corresponding to each peak of the DRT spectra obtained from EIS measurements, tests were undertaken at three different temperatures: 650, 675, and 700 °C. The molar fraction of hydrogen at the anode varied from 10% to 90% (10/20/50/90%—air at the cathode) and the cathode oxygen content from 4% to 21% (4/6/8/10/21%—at constant 90% hydrogen at the anode) by diluting the air feed with N_2. The operating conditions' variation range was chosen as an overall compromise between (i) relevant operating conditions that are similar to the ones potentially used in real applications; (ii) inducing evident impedance variations; (iii) avoiding conditions that could cause the irreversible degradation of the sample (e.g., fuel or oxidant starvation); (iv) technical and time limitations of the experimental setup. Each condition is stabilized prior to the EIS measurement. The reason for using high hydrogen content is to maintain low hydrogen-related resistances, decreasing their overlap with oxygen-related resistance. Table 2 summarizes all the gas compositions measured at three different temperatures represented in molar fractions.

Table 2. The gas composition of different measurement stages in molar fractions.

T 650, 675, 700 °C		Hydrogen Variation				Oxygen Variation				
		1	2	3	4	1	2	3	4	5
Anode gases	H_2	0.10	0.20	0.50	0.90	0.90	0.90	0.90	0.90	0.90
	N_2	0.90	0.80	0.50	0.10	0.10	0.10	0.10	0.10	0.10
Cathode gases	O_2	0.21	0.21	0.21	0.21	0.04	0.06	0.08	0.10	0.21
	N_2	0.79	0.79	0.79	0.79	0.96	0.94	0.92	0.90	0.79

2.2. Tool Development

A tool was developed in a MATLAB environment to identify the peaks of the DRT spectra diagram and quantify these peaks' shifts as a function of the change in operating conditions. The program operation could be divided into several functions, which are (i) peak identification, (ii) frequency region definition, and (iii) peak shift quantification. In

addition, specific functions were coded to categorize and illustrate the results in different process stages. Figure 3 illustrates the overall workflow of the tool.

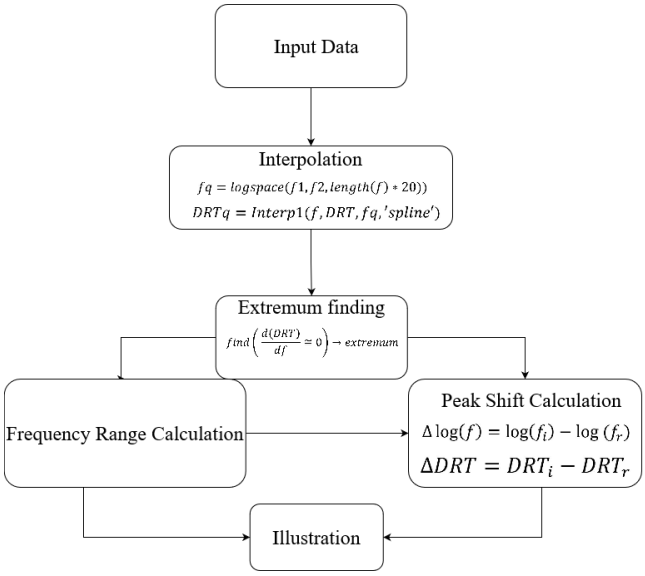

Figure 3. Workflow of the main functions of the tool.

The first objective is peak identification: the discrete DRT data calculated from the experiments were imported to the program as two vectors (frequency and corresponding DRT). These two vectors went through interpolation before being inserted into the main functions of the program in order to operate with continuous data and avoid incorrect peak identification merely due to the discrete form of the experimental data points. The interpolation methods considered for this goal are linear and spline interpolation. The query points generated for the interpolation follow a logarithmic spacing to correlate with the distribution of DRT values in each decade of frequency.

The interpolated frequency and DRT vectors are the inputs of a peak identification function that searches for the minimum and maximum points of the DRT value by calculating the first derivative of the DRT and finding the points where the sign of the derivative values changes from positive to negative (for maximum points) or vice versa (for minimum points). Thus, a point in the DRT is indexed as maximum or minimum with the nearest value of the first derivative to zero (Equation (1)). Interpolated data allows estimating extremum points that are not necessarily equal to the experimental measurements, improving the analysis capability of the tool.

$$find\left(\frac{d(DRT)}{df} \cong 0\right) \rightarrow extremum \quad (1)$$

Since the extremum finding function could identify a different number of peaks than the actual underlying processes, it is advisable to provide the characteristic frequency bandwidths of each physicochemical process (in which each peak can shift) as an input to correctly categorize the peaks and restrict the peak shifting quantification in said bandwidths. The characteristic frequency bandwidths are provided with an iterative procedure based on an initial guess of evenly distributed processes, which is subsequently updated with the actual characteristic frequency bandwidths, calculated as the frequency range between the two minimum points adjacent to a maximum point.

The iterative steps taken to calculate the frequency bandwidths are as follows (Figure 4):

- First, each data set's maximum and minimum points were extracted from the index provided by the extremum finding function.
- Then, a pre-allocation of possible frequency bandwidths is defined considering seven peaks logarithmically distributed. The reason for having seven pre-allocated peaks

relies on the fact that the polarization resistance of a SOFC sample is typically composed of six different processes (two anode charge transfer processes P1 & P2, one cathode charge transfer process P3, one anode mass transfer process P4, one cathode mass transfer process P5, one anode gas conversion process P6) which lead to a DRT response composed of seven peaks (also considering the satellite peak P4' related to the anode mass transfer process) [35].

- Next, the maximum points present within each frequency range are identified, and the average frequency of said maximum points is calculated.
- Minimum points are searched between each maximum point obtained in the previous step. The frequency ranges between the average minimum points adjacent to a maximum point are calculated and represent the calculated characteristic frequency ranges for each physicochemical process (P1 to P6) which update the previous pre-allocation.

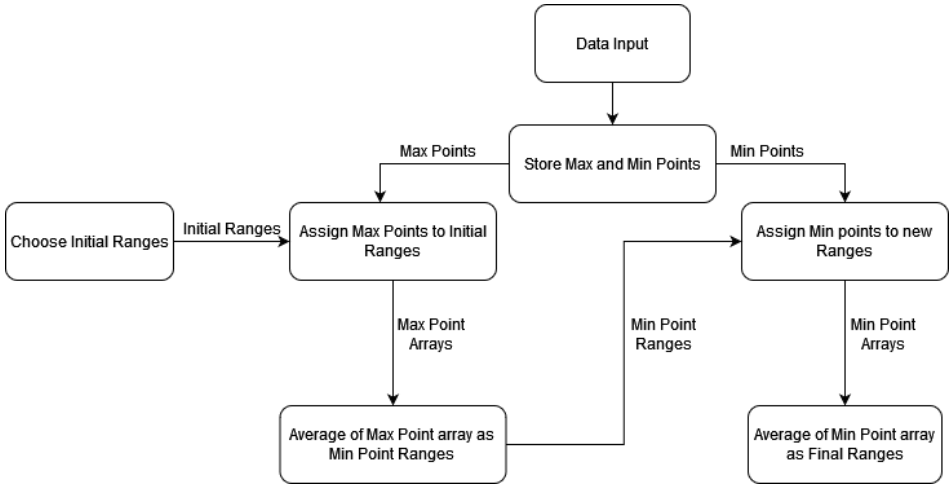

Figure 4. Frequency bandwidth calculation procedure.

Once the frequency bandwidths are defined, the shift in the frequency (Δf—logarithmic) and DRT (ΔDRT) values of peaks falling in the same operating bandwidth were calculated for each variation of operating conditions vis-à-vis the values in reference conditions (hydrogen content is 50%, oxygen content is 21% (Air), and temperature is 700 °C (StdCond)). By assessing the terms Δf and ΔDRT, it is possible to quantify the degree of dependency of each specific peak to the variation of operating conditions (identifying, for example, temperature or gas composition dependencies of each peak). Finally, an illustration window provides a comprehensive overview of the DRT curves accompanied by the frequency bands and numerical shift results, which are represented in tables.

It is noteworthy that in the current status of the tool, several errors may occur (e.g., two peak points of one operating condition may fall in the same frequency band, etc.). These sorts of errors—the most frequent of which are reported in the results section—are currently solved manually by post-processing after analyzing the results.

2.2.1. Tool Performance Indicator

The performance assessment indicator idx_{tool} was introduced to assess the goodness of the tool, where idx_{tool} is equal to the number of peaks that were correctly interpreted by the tool divided by the actual physicochemical processes occurring in the cell (Equation (2)), separately evaluated for each process (P1 to P5; in OCV conditions P6—which is related to gas conversion—is not present due to the absence of current flow) under different operating conditions. The obtained results are expressed in percentages to indicate the tool's success rate in calculating the peak shift for each peak. The average value of idx_{tool} is calculated for each batch to assess the tool performance at the batch level.

$$idx_{tool} = \frac{number\ of\ peaks\ correctly\ identidified\ by\ the\ tool}{number\ of\ actual\ peaks} \quad (2)$$

3. Results

3.1. Qualitative Physicochemical Process Identification by DRT Visual Inspection

The experimental dataset on which the analysis is based is composed of a complete parametrical characterization of three cell production batches (23 samples in total, at least 5 cells/batch). The electrochemical characterization results in StdCond (in terms of polarization curves, power density curves and EIS data) are reported in Figure 5.

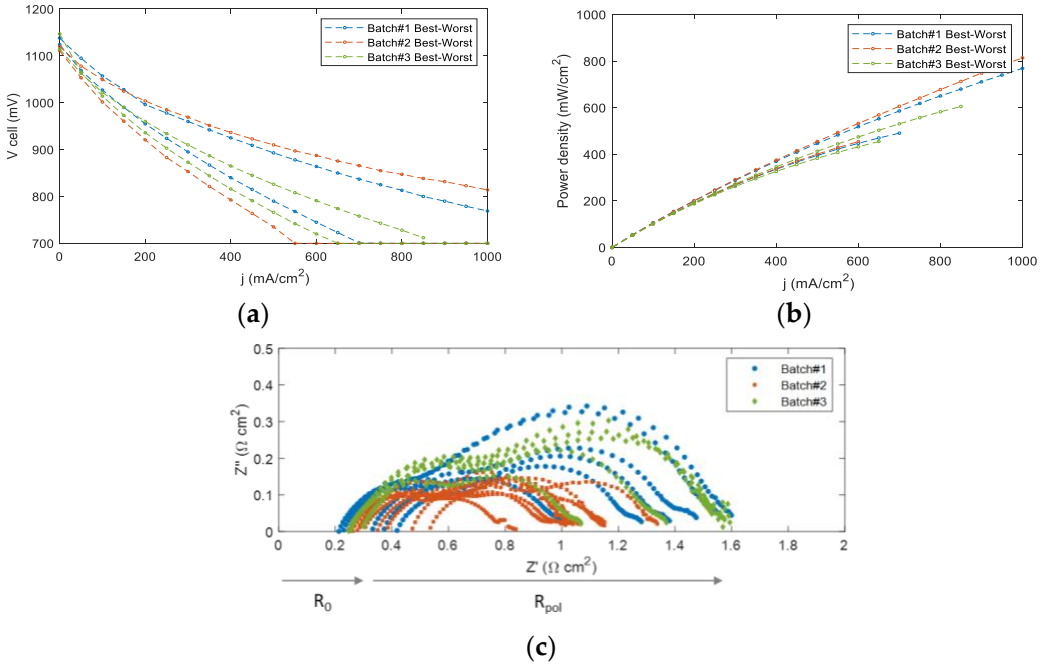

Figure 5. Experimental data (StdCond)—(**a**) IV curves; (**b**) power density curves and (**c**) EIS measurements; from [25].

Summary of Process Identification

Although process identification analysis was performed for all samples, for brevity, in the following subsections, selected representative samples are presented that show typical DRT shifts with the parametric variation of operating conditions. The process identification was performed on cells of a single batch to ensure the most similar characteristics. The detailed procedure is presented in Appendix A. Overall, it can be stated that:

- process P1 is related to the transport of O^{2-} ions within the YSZ matrix of the anode functional layer;
- process P2 is identified with the charge transfer mechanism of the electrochemical oxidation of the fuel occurring within the anode functional layer in the triple-phase boundary (TPB) region;
- process P3 has been ascribed to the charge transfer mechanism for the reduction of O_2 to O^{2-} at the cathode side;
- process P4 consists of a principal peak at the characteristic frequency followed by a smaller P4' at a higher frequency in the DRT plots. This process is associated with a mass transport phenomenon, or rather to the gas diffusion through the open porosity of the anode substrate;
- process P5 in the lowest frequency region can be associated with the cathodic gas diffusion in the porous structure;
- process P6, related to gas conversion, is not observed in the analyzed campaign since the EIS measurements are performed in OCV conditions; thus, no gas conversion occurs.

The results of the process identification analysis are in good accordance with the existing literature on comparable cell designs and characteristics [36–38].

3.2. Software Tool Results—Quantitative DRT Analysis

To demonstrate the capability of the developed tool, the experimental DRT spectra of the three batches were analyzed to verify whether similar conclusions could be drawn with the developed tool. It should be noted that, for the sake of brevity, the numerical results (Sections 3.2.1 and 3.2.2) are related to the average values obtained from all the tested samples. Full results for each cell and batch can be found in the Supplementary Materials.

A similar process identification analysis is carried out by comparing DRT spectra under parametric variation of operating conditions. The variations were analyzed, considering StdCond as a reference. However, thanks to the automated DRT analysis tool, the results can be assessed quantitatively and not only qualitatively, as for the case of visual inspection. Figures 6–8 illustrate the output panel of the tool in relation to hydrogen content, temperature, and oxygen content variations, respectively.

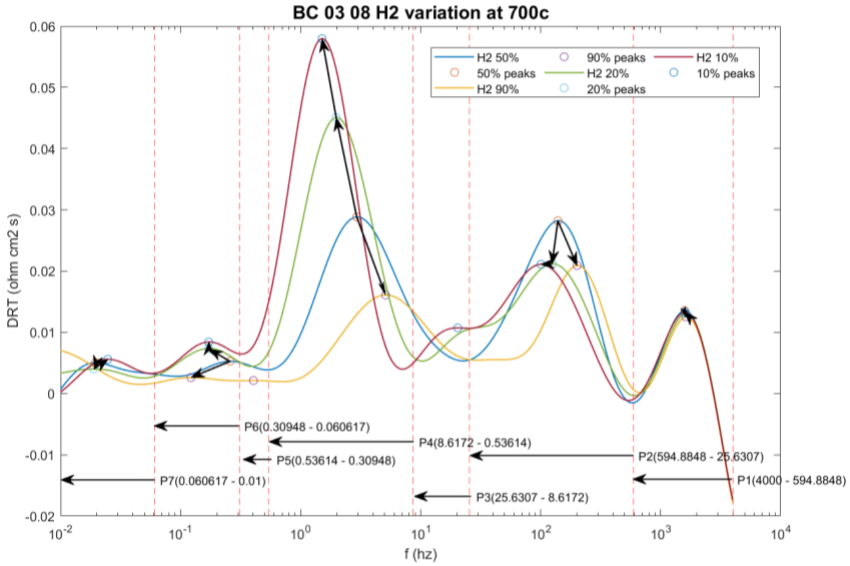

Figure 6. Tool user interface illustrating hydrogen variation analysis.

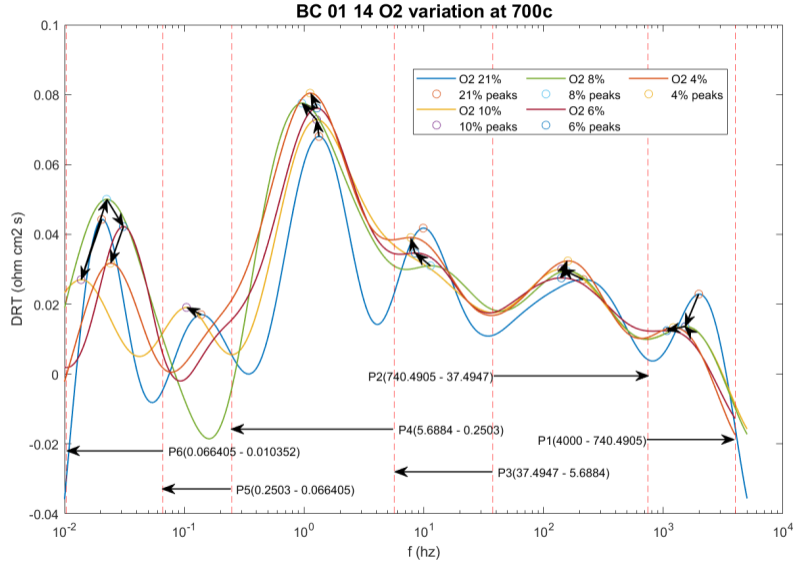

Figure 7. Tool user interface illustrating oxygen variation analysis.

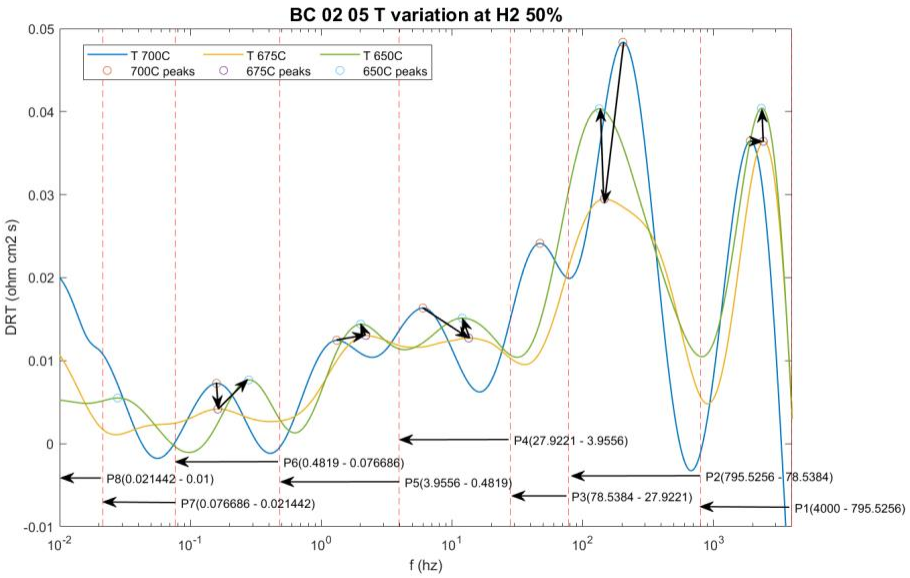

Figure 8. The tool user interface illustrating temperature variation analysis.

3.2.1. Hydrogen Partial Pressure Variation

The hydrogen variations (Figure 6) show that the peak amplitude around 1 Hz (P4 hydrogen mass diffusion in the anode substrate) reacts to variations in anode gas hydrogen content percentage with a variation in DRT amplitude by 0.02 Ohm·cm^2·s and a frequency shift of 0.12 log(Hz) on average. Other peaks remained unchanged or showed minor changes with less than 0.004 Ohm·cm^2·s average change.

3.2.2. Oxygen Partial Pressure Variation

The oxygen variation (Figure 7) was analyzed with a temperature of 700 °C and hydrogen content of 90% as a reference. A considerable effect is seen in the frequency of the cathode charge transfer region around 100 Hz (P3) of 0.082 log(Hz) on average. The tool's analysis of the lowest frequency region peak (oxygen mass diffusion in the cathode layer) was relatively difficult due to uncertainties accompanying the low-frequency measurement. However, it is apparent that an affected area due to cathode gas oxygen variation is the one with the low-frequency peaks with an average variation of 0.068 log(Hz) and 0.003 Ohm·cm^2·s, despite the fact that the oxygen variation increment is smaller than the two other variations.

3.2.3. Temperature Variation

Finally, the temperature variation analysis (Figure 8) shows that the peaks affected by temperature variation are located in the higher frequency region (around 100–4000 Hz). P1 and P2 deviated by an average of 0.086 log(Hz) and 0.14 log(Hz) in frequency and 0.004 Ohm·cm^2·s and 0.008 Ohm·cm^2·s in DRT, respectively. This is in accordance with the process identification findings, which states that high-frequency peaks are related to thermally activated physicochemical processes.

3.2.4. Peak Frequency Range Calculation

It is essential to distinguish the operating frequency range of each physicochemical process in the DRT spectra to ascribe each DRT peak to a process. In previous works, the frequency range of each DRT peak was determined by visual interpretation as part of a process identification procedure. It is generally accepted that the DRT peaks related to each process are located at each decade of the frequency span. However, calculating the frequency ranges using the developed tool enables the quantitative analysis of the characteristic frequency bandwidths of each process.

As a result of the peak frequency range calculation, the actual frequency range of each peak for each batch was calculated (Figure 9), which is slightly shifted with respect to the pre-allocated ones. It is noteworthy that the calculation was limited to between 0.01 Hz and 4000 Hz, since this is approximately the total range of the measured EIS data. Peak P1 (oxygen ion transfer in the anode functional layer) is located in the higher frequency portion of the DRT spectra (750–4000 Hz—average). Peaks P2 (fuel oxidation charge transfer mechanism) and P3 (oxygen reduction charge transfer mechanism in the cathode layer) often appeared convoluted and hardly distinguishable by the tool despite occupying two decades in the frequency range (35–750 Hz—average). Process P4 (hydrogen mass diffusion in the anode substrate) appears as two peaks, and for this work only the main peak at a lower frequency (0.35–9.88 Hz—average) was considered for analysis. Finally, P5 (oxygen mass transport at the cathode layer) appears at the lowest frequency (0.01–0.5 Hz—average). Overall, the numerical result provided by the tool complies with the visual location of the operating frequency ranges of the physicochemical processes in the DRT spectra. Table 3 summarizes the results of this section. Full frequency range results for each cell can be found in the Supplementary Materials.

(**a**) (**b**)

Figure 9. Comparison of frequency ranges of each process. (**a**) Visual inspection of DRT peaks. (**b**) Calculated by the tool.

Table 3. Frequency ranges calculated for each batch at every parameter variation.

		P1		P2 + P3		P4		P5	
		Max (Hz)	**Min (Hz)**	**Max (Hz)**	**Min (Hz)**	**Max (Hz)**	**Min (Hz)**	**Max (Hz)**	**Min (Hz)**
Visual inspection		10,000	1000	1000	10	10	1	1	0.01
Batch 1	**H_2 var**	4000	761.210	761.210	30.880	5.610	0.300	0.050	0.010
	O_2 var	4000	775.350	775.350	40.720	6.280	0.340	0.050	0.010
	T var	4000	878.040	878.040	30.410	4.950	0.290	0.060	0.010
	Avg	4000	804.860	804.860	34.000	5.610	0.310	0.050	0.010
Batch 2	**H_2 var**	4000	707.490	707.490	35.920	9.400	0.360	0.050	0.010
	O_2 var	4000	752.800	752.800	53.460	7.590	0.410	0.050	0.010
	T var	4000	802.800	802.800	39.200	12.140	0.410	0.060	0.010
	Avg	4000	754.360	754.360	42.860	9.710	0.390	0.050	0.010
Batch 3	**H_2 var**	4000	650.140	650.140	24.510	5.770	0.290	0.060	0.010
	O_2 var	4000	719.390	719.390	41.250	23.790	0.410	0.050	0.010
	T var	4000	720.860	720.860	20.980	13.360	0.320	0.060	0.010
	Avg	4000	761.210	761.210	30.880	5.610	0.300	0.050	0.010

The average frequency ranges of the high-frequency processes (P1, P2, and P3) for Batch 3 seem slightly shifted towards lower frequencies with an average shift of around 50–100 Hz for P1 and around 10 Hz for P2 + P3 with respect to the other batches. This frequency shift might be related to the modification of the AFL, as mentioned in [25].

3.2.5. Peak Shift Calculation Results

The numerical results of the peak shift calculation for the three batches are reported in Tables 4–6 and Figures 10–12. The results are obtained by calculating the average peak

shifts of all batch samples for every operating condition variation in terms of frequency and DRT change. The detailed numerical results of the frequency and DRT shifts for all cells are shown in the Supplementary Materials.

Table 4. Frequency and DRT amplitude change due to hydrogen variation at 700 °C and O_2 21%. *REF.* stands for the reference value.

		P1		P2 +P3		P4		P5	
H_2 Variations		**Δf (log(Hz))**	**ΔDRT (Ohm cm^2 s)**	**Δf (log(Hz))**	**ΔDRT (Ohm cm^2 s)**	**Δf (log(Hz))**	**ΔDRT (Ohm cm^2 s)**	**Δf (log(Hz))**	**ΔDRT (Ohm cm^2 s)**
Batch 1	**H_2 10%**	0.00024	−0.00182	−0.0632	0.01246	−0.06873	0.02879	−0.0512	0.00856
	H_2 20%	0.02351	0.00136	−0.1401	0.00613	−0.04254	0.01786	0.05333	0.00169
	H_2 50%	*REF.*	*REF.*	*REF.*	*REF.*	*REF.*	*REF.*	*REF.*	*REF.*
	H_2 90%	0.0095	0.00087	0.09303	−0.00847	0.12523	−0.02693	−0.09968	0.00863
Batch 2	**H_2 10%**	−0.0078	−0.00016	−0.12833	0.00306	−0.13895	0.03138	−0.08287	0.00332
	H_2 20%	−0.00432	−0.0002	−0.08506	0.00024	−0.06579	0.00933	−0.10673	−0.00257
	H_2 50%	*REF.*	*REF.*	*REF.*	*REF.*	*REF.*	*REF.*	*REF.*	*REF.*
	H_2 90%	−0.03067	−0.00114	0.0038	−0.00148	0.15714	−0.01081	−0.0767	0.00106
Batch 3	**H_2 10%**	0.01442	0.00028	−0.11518	−0.00203	−0.27474	0.03248	0.16255	−0.00071
	H_2 20%	0.01762	0.00025	−0.07906	0.00019	−0.11352	0.0169	−0.01485	−0.00093
	H_2 50%	*REF.*	*REF.*	*REF.*	*REF.*	*REF.*	*REF.*	*REF.*	*REF.*
	H_2 90%	0.00484	−0.00094	0.0997	−0.00246	0.05436	−0.00885	0	0

Table 5. Frequency and DRT amplitude change due to oxygen variation at 700 °C and H_2 90%. *REF.* stands for the reference value.

		P1		P2 + P3		P4		P5	
O_2 Variations		**Δf (log(Hz))**	**ΔDRT (Ohm cm^2 s)**	**Δf (log(Hz))**	**ΔDRT (Ohm cm^2 s)**	**Δf (log(Hz))**	**ΔDRT (Ohm cm^2 s)**	**Δf (log(Hz))**	**ΔDRT (Ohm cm^2 s)**
Batch 1	**O_2 4%**	−0.01021	−0.00317	−0.13864	0.00514	−0.02591	0.01841	0.10527	−0.00383
	O_2 6%	−0.02134	−0.00234	−0.13727	0.00728	0.00576	0.01574	0.06843	0.00527
	O_2 8%	0.02871	−0.00199	−0.19766	0.00487	0.02269	0.01266	0.01488	0.00418
	O_2 10%	−0.01311	−0.00252	−0.09944	0.00587	0.02464	0.00861	−0.0638	−0.00669
	O_2 21%	*REF.*	*REF.*	*REF.*	*REF.*	*REF.*	*REF.*	*REF.*	*REF.*
Batch 2	**O_2 4%**	0.00031	0.00114	−0.01819	0.00258	0.00503	0.01261	0.10391	0.0024
	O_2 6%	0.01186	0.00068	0.0644	0.00205	0.08501	0.00962	0.00858	0.00164
	O_2 8%	0.02865	−0.0002	0.08204	−0.00068	0.05572	0.00711	−0.10564	0.00221
	O_2 10%	−0.00891	−0.00017	0.02605	0.00139	−0.06579	0.00402	0.11671	0.00337
	O_2 21%	*REF.*	*REF.*	*REF.*	*REF.*	*REF.*	*REF.*	*REF.*	*REF.*
Batch 3	**O_2 4%**	0.03332	0.00069	−0.08248	0.00279	0.03538	0.00404	−0.0825	0.00173
	O_2 6%	0.01688	0.00064	−0.03354	0.00097	0.03592	0.00259	−0.01315	0.00057
	O_2 8%	0.01348	0.00088	−0.04386	0.00201	0.04426	0.00237	−0.1135	0.00072
	O_2 10%	0.0364	0.00068	−0.06012	0.00051	−0.0207	0.00272	0.01307	0.00107
	O_2 21%	*REF.*	*REF.*	*REF.*	*REF.*	*REF.*	*REF.*	*REF.*	*REF.*

Hydrogen Variation

By decreasing the hydrogen content of the anode gas, the frequency of P4 and P3 + P2 decreased by 0.12 log(Hz) and 0.09 log (Hz), respectively. P4 is the most affected peak with a DRT amplitude increase of around 0.02 Ohm.cm^2.s under 10% hydrogen conditions. The opposite happened to these peaks when the hydrogen content increased to 90%. The quantitative results are coherent with the qualitative ones, where an increased hydrogen content represents more fuel for the SOFC, improving all anode processes (both charge and mass transfer). The other peaks showed no significant dependence on hydrogen variation.

The frequency reduction observed with a reduction in hydrogen concentration might be related to the influence of surface chemistry on the complex EIS. For more details see [36].

Table 6. Frequency and DRT amplitude change due to temperature variation at H_2 50% and O_2 21%. *REF.* stands for the reference value.

		P1		P2 + P3		P4		P5	
T Variation		**Δf (log(Hz))**	**ΔDRT (Ohm cm^2 s)**	**Δf (log(Hz))**	**ΔDRT (Ohm cm^2 s)**	**Δf (log(Hz))**	**ΔDRT (Ohm cm^2 s)**	**Δf (log(Hz))**	**ΔDRT (Ohm cm^2 s)**
Batch 1	**650 °C**	0.10386	0.01244	−0.21054	0.02517	−0.0062	−0.00174	0.03645	0.00352
	675 °C	0.05403	0.00809	−0.08379	0.01538	−0.01321	−0.00527	0.09194	0.00057
	700 °C	*REF.*	*REF.*	*REF.*	*REF.*	*REF.*	*REF.*	*REF.*	*REF.*
Batch 2	**650 °C**	0.12099	0.0123	−0.05802	0.01605	0.07017	0.00206	0.07141	−0.00245
	675 °C	0.03816	0.00606	0.0054	0.00681	0.01165	0.00064	0.07552	−0.00429
	700 °C	*REF.*	*REF.*	*REF.*	*REF.*	*REF.*	*REF.*	*REF.*	*REF.*
Batch 3	**650 °C**	0.1427	0.00608	−0.25314	0.02044	−0.00862	0.00125	0.07226	0.00714
	675 °C	0.05364	0.00472	−0.23212	0.01317	−0.09156	0.00175	0.0962	0.00208
	700 °C	*REF.*	*REF.*	*REF.*	*REF.*	*REF.*	*REF.*	*REF.*	*REF.*

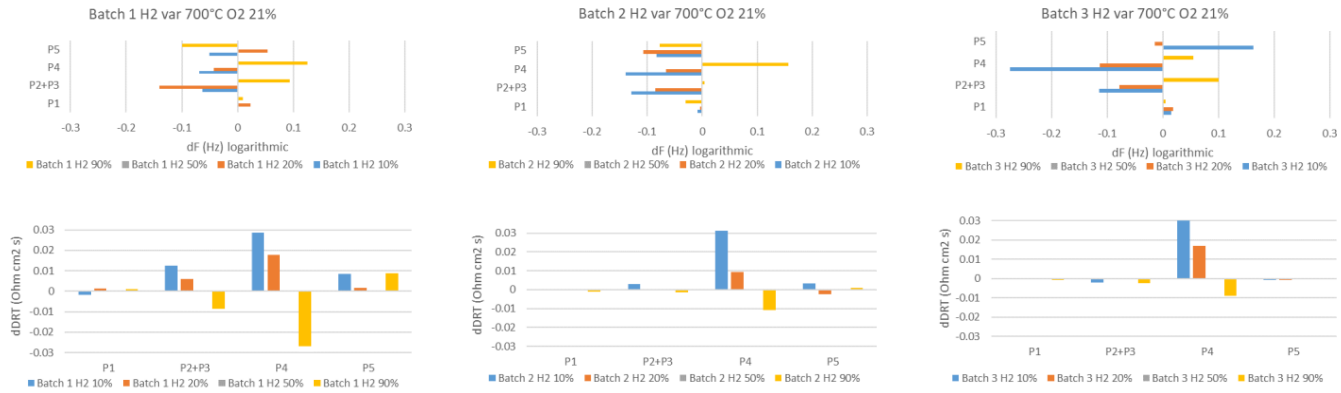

(**a**) (**b**) (**c**)

Figure 10. Frequency and DRT change due to hydrogen variation at 700 °C and O_2 21%. (**a**) Batch 1. (**b**) Batch 2. (**c**) Batch 3.

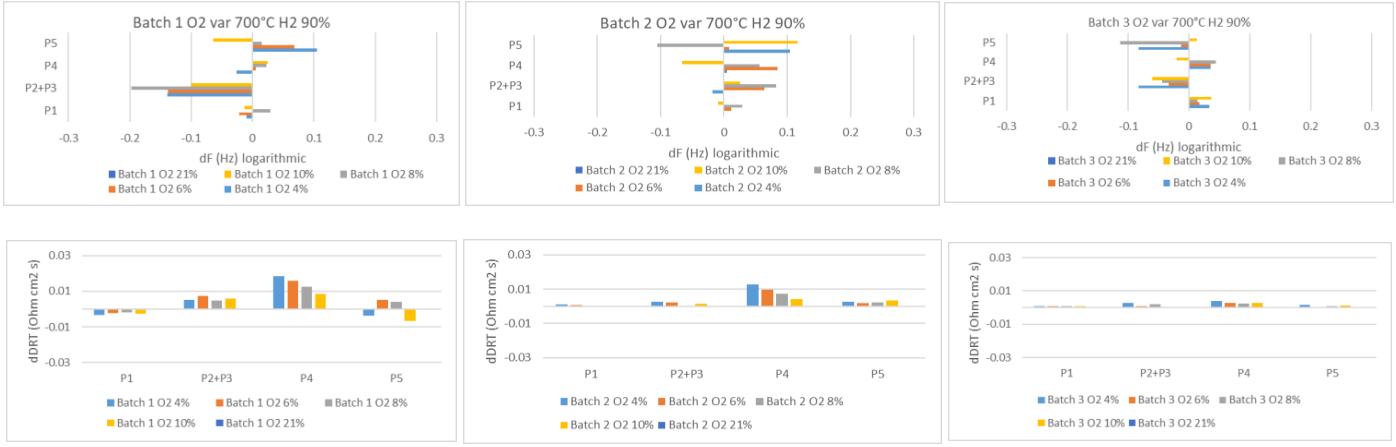

(**a**) (**b**) (**c**)

Figure 11. Frequency and DRT change due to oxygen variation at 700 °C and H_2 90%. (**a**) Batch 1. (**b**) Batch 2. (**c**) Batch 3.

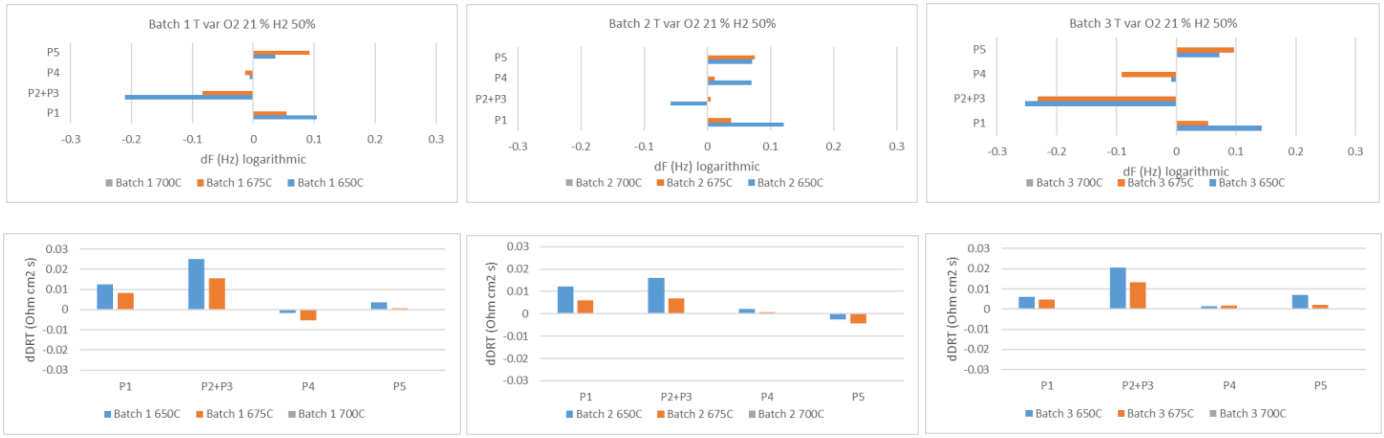

(**a**) (**b**) (**c**)

Figure 12. Frequency and DRT change due to temperature variation at H_2 50% and O_2 21%. (**a**) Batch 1; (**b**) Batch 2; (**c**) Batch 3.

Batch 3 shows a relevant increase in the frequency shift, especially for the peak P4 (up to almost 0.3 log(Hz) in H_2 10% conditions). No significant differences in DRT shift trends are observed between batches. The different frequency shifts observed for Batch 3 could be potentially related to the change in porosity resulting from a modified AFL (not only in terms of pore number but also in relation to their shape and size), which could affect the gas diffusion mechanisms in the anode. However, no further statements can be provided in the absence of more detailed information.

Oxygen Variation

By decreasing the oxygen content of the cathode gas from 21% to 4%, the peaks fluctuated in terms of frequency change (around 0.1 log(Hz)). While these changes were not similar among the three analyzed batches, it could be concluded that the most affected peaks were P5 and P2 + P3. In terms of the DRT amplitude change, oxygen variation slightly increased the overall DRT amplitude of most of the peaks (around 0.08 Ohm cm^2 s). Among them, P4, which is related to hydrogen mass diffusion, was also affected. The absence of a clear trend in the quantitative results is potentially related to the limited variation range of the oxygen content (4–21%), which does not induce significant variations in the processes' impedance. Studies show that significant performance variations are obtained only in extremely oxygen-depleted oxidant flows (<4% oxygen) [39]. However, the influence of oxygen variation on the anode diffusion peak (P4) somehow suggests a connection between the oxygen flow at the cathode and the anode processes.

The frequency shifts among different batches do not follow a common trend, mainly due to the small shifts caused by oxygen variation in the DRT. A slightly lower dependency of the DRT amplitude variation on oxygen content was found for Batch 3. However, this can be ascribed to fluctuations in the measurement signal.

Temperature Variation

Temperature variation mostly affected the high-frequency peaks (around 1000 Hz), P1, and P2 + P3. In terms of frequency, P1 and P2 + P3 experienced a frequency increase (0.086 log(Hz)) and decrease (−0.14 log(Hz)), respectively. Although it does not represent a thermally activated process, P5 also slightly decreased in frequency (0.07 log(Hz)). Concerning the DRT amplitude, decreasing the temperature increased the value of P1 (0.008 Ohm cm^2 s) and P2 + P3 (0.016 Ohm cm^2 s) while having a negligible effect on the other peaks, which is consistent with the identification of P1, P2, and P3 with thermally activated charge transfer processes.

In terms of frequency shifts, Batch 3 shows a similar trend to Batch 1, while Batch 2 seems to show a lesser dependency on temperature compared to the other batches. Instead, in terms of DRT shifts, Batch 3 shows a smaller dependency of P1 on temperature variations with respect to Batch 1 and Batch 2.

3.3. Tool Errors and Post-Processing

This section explains the most common errors encountered when operating the program. These errors raise the issue of the importance of a post-processing procedure to eliminate some of the errors as far as reasonably possible. Some of these errors result from measurement inaccuracies (e.g., low-frequency EIS measurements) while others are the result of the data analysis methods (e.g., small change of curvature in the DRT spectra not identified by the first derivative method). Implementing a post-processing procedure is necessary before starting the interpretation phase to reach more accurate findings.

3.3.1. Missed Peaks

The program may miss an extremum point in a specific DRT data set in the phase of peak identification. The main reason for this error is due to the fact that the curvature of the DRT data is shaped in a form in which the first derivative does not evidently change from positive to negative. There are two physical phenomena behind this error. When two processes have very close or overlapping characteristic frequencies, they might appear convoluted. The other phenomenon occurs when the contribution of a physicochemical process in the DRT spectra becomes so small with respect to other peaks that it forms a flat shape that is not similar to a Gaussian curve (e.g., anodic processes with very high hydrogen content). These two conditions might make the peak indistinguishable for the tool.

3.3.2. Extra Frequency Regions

One of the main errors that can appear is the calculation of extra frequency regions. The reason for this error is the difference between the number of identified peaks and the actual number of underlying physicochemical processes. Although this might be the result of the natural behavior of the DRT dataset with the variation of operating conditions, it affects the frequency band calculation function. The tool takes the maximum number of peaks identified in a measurement data set (up to eight peaks) as a reference and categorizes the minimum points that fall between every two maximum points. This can produce a higher number of frequency regions according to the number of incorrectly identified peaks, while the maximum number of frequency regions needed is five, related to the number of separate underlying processes (considering P2 + P3 often convoluted). The user interference is used to manually distinguish between necessary and unnecessary frequency lines and to choose the needed frequency ranges for further analysis; thus, prior knowledge of the physicochemical processes is required.

3.3.3. Missed Peak Shift Calculation

When a peak falls into a different frequency region with respect to the related reference peak of the same process (as a result of extra frequency ranges or due to high mobility of a peak as a consequence of specific operating conditions), the tool considers it unrelated to the same process and does not calculate its frequency and DRT difference.

3.3.4. Convolution of Oxygen Charge Transfer in the Anode and Cathode Layers

As previously mentioned, some errors are inherently related to the specifics of the experimental input data provided and analyzed by the tool. One of these errors is produced in relation to oxygen ion transport in the anode functional layer (P2) and charge transfer of the oxygen reduction reaction in the cathode layer (P3) processes. In most samples, these two peaks appear convoluted in the DRT spectra, and are thus hidden from the distinctive capability of the tool. It is worth mentioning that distinguishing between these two peaks in the case of convolution is not easy for a user and requires prior knowledge and comparison

with other data sets obtained from the sample. For this reason, part of the quantitative results is given for the process of the couple P2 + P3 together.

3.3.5. Anode Gas Diffusion Region Peaks

Another error that originates from the shape of the DRT spectra is related to the hydrogen diffusion in the anode layer, which appears, as discussed before, as two peaks: one main peak with a high DRT value at a lower frequency (P4) and an adjacent peak at a higher frequency with a lower DRT value (P4′) which are explained, as discussed previously, as the typical Warburg impedance response results (a principal peak, falling at the characteristic frequency of the process, followed by a set of satellite peaks), which is representative of the gas diffusion process. These two peaks, which are related to a single phenomenon and shown to deviate likewise, are considered two different processes by the tool calculation and are therefore gathered in different groups, and separate frequency ranges are calculated for them. This error is handled efficiently by disregarding the smaller peak P4′ in the peak identification, frequency range, and peak shift calculation [40].

3.3.6. Cathode Gas Diffusion Region

The cathode gas diffusion region is located in the lower frequency portion of the DRT spectra (between 0.1 and 0.01 Hz) [12], and it is often accompanied by high measurement error and noise/scattering due to the low frequency of impedance measurement [15]. In this frequency region, it has been observed that in some cases, only one peak related to cathode gas diffusion appears, while in some other cases there are two peaks. This inconsistency results in peak shift calculation mistakes since the tool cannot correctly detect related peaks nor group them appropriately. Overall, the cathode diffusion region results are not crucial since its impedance contribution is very low compared to the contribution of other physicochemical processes.

3.3.7. Post-Processing

As discussed in the previous subsections, in most cases, the tool's outcome needs to be checked to identify probable errors in the results and manually eliminate them. Therefore, the tool's outcome is not readily usable as a turnkey solution but rather an integrated tool in electrochemical impedance data analysis. Without this post-processing stage, it is impossible to draw meaningful interpretations from the tool's calculation without a pre-defined physical background. This process is done manually and requires knowledge about the physicochemical processes related to the DRT spectra, which are gained through experience in process identification.

3.4. Tool Performance Results

The results of the performance indicator evaluation idx_{tool} (introduced in Section 2.2.1), presented in Table 7, show that the tool performs well overall with an average value of idx_{tool} (for all processes) around 90% (between 88–92%). The tool performs best when identifying the higher frequency peaks correctly (average idx_{tool} equal to 100% for P1 and 98.25% for P2 + P3) with respect to lower frequency peaks (average idx_{tool} equal to 98.12% for P4 and 63.36% for P5). This is because the impedance measurement at lower frequencies (characteristic of P5) is affected by more noise, as discussed in Section 3.3.6. Although high idx_{tool} values are obtained for P2 + P3, this is mainly due to the fact that the two processes have been grouped, due to the typical convolution of the two peaks, as discussed in Section 3.3.4. However, if the performance indicator had been calculated on the two peaks separately, lower idx_{tool} values would have been obtained due to the inability of the tool to discern between the two convoluted peaks.

Table 7. Summary of tool performance idx_{tool} results.

	P1	P2 + P3	P4	P5	Global
Batch 1	100.00%	100.00%	98.41%	68.25%	91.67%
Batch 2	100.00%	96.97%	95.96%	59.60%	88.13%
Batch 3	100.00%	97.78%	100.00%	62.22%	90.00%

4. Conclusions

In the context of this work, a custom numerical analysis tool was developed to analyze the deconvoluted EIS results obtained from SOFC testing by means of the DRT method. The developed tool allows for the automated and quantitative interpretation of DRT spectra and their shifts with variations in operating conditions. The proposed tool's novelty is overcoming qualitative DRT interpretation to better relate the EIS data to the SOFCs' underlying physicochemical processes.

The DRT analysis tool was developed in a MATLAB environment in three steps: (i) identification of the DRT peaks based on analysis of the first derivative of the interpolated DRT function, (ii) iterative characteristic frequency region definition for each physicochemical process, and (iii) peak shift quantification (both in logarithmic frequency and in DRT amplitude) with respect to reference conditions.

The developed tool is applied to a vast experimental DRT dataset related to an extensive campaign carried out on 23 SOFC button-sized samples from three production batches in which EIS measurements (and subsequent DRT calculations) are performed in OCV conditions while performing parametric variations of operating conditions (hydrogen content, oxygen content, temperature). The performance and results of the tool are compared with qualitative DRT interpretation by visual inspection in previous works to validate the approach preliminarily.

The DRT analysis tool was able to identify DRT peaks related to the main SOFC physicochemical processes (overall idx_{tool} around 90%). The main issues that affect the tool performance are related to the peak convolution (high-frequency peaks P2 and P3 between 50–1000 Hz), the low impact of operating conditions and signal noise (P5 at very low frequencies < 0.1 Hz), the presence of satellite peaks (P4' and P4), and others. Different post-processing approaches were implemented to deal with each issue.

It was possible to calculate each process's actual characteristic frequency range, providing additional information with respect to the qualitative analysis. The quantitative peak shifts were calculated automatically and illustrated to help interpret the analyzed data, corroborating the assignment of physicochemical processes to each of these peak points (e.g., the high-frequency peaks P1, P2, and P3 related to thermally activated charge transfer processes; the low-frequency peak P4 and P5 related to diffusion in the electrodes). In terms of frequency and amplitude, the calculated peak shifts showed consistency with the process identification based on the qualitative interpretation of DRT spectra. It was possible to identify minor changes in the shifts of Batch 3 with respect to other batches.

The successful deployment of the developed DRT analysis tool opens new possibilities for SOFC characterization and monitoring, implementation in degradation studies, and the development of tailored and verifiable testing protocols.

Supplementary Materials: The following supporting information can be downloaded at: https://www.mdpi.com/article/10.3390/en15103702/s1, Table S1. Batch 1 Frequency Band Calculation; Table S2. Batch 1 Shift Results; Table S3. Batch 2 Frequency Band calculation; Table S4. Batch 2 Shift Results; Table S5. Batch 3 Frequency Band calculation; Table S6. Batch 3 Shift Results.

Author Contributions: Conceptualization, A.M.F. and S.J.M.; methodology, A.M.F., M.A., M.D.P. and D.P.; experimental, D.P. and M.D.P.; software, M.A.; validation, M.A. and D.P.; resources, S.P.; data curation, D.P. and A.M.F.; writing—original draft preparation, M.A.; writing—review and editing M.A., A.M.F., D.P. and M.D.P.; visualization, M.A. and A.M.F.; supervision, S.J.M., S.P. and D.B.; project administration, S.J.M.; funding acquisition, S.J.M. All authors have read and agreed to the published version of the manuscript.

Funding: This research was funded by the EU project qSOFC (Horizon 2020; Grant ID: 735160).

Institutional Review Board Statement: Not applicable.

Informed Consent Statement: Not applicable.

Data Availability Statement: The detailed results of the DRT analysis tool for each sample and operating condition are reported in the Supplementary Materials.

Acknowledgments: This research was funded by the EU project qSOFC (Horizon 2020 Fuel Cells and Hydrogen Joint Undertaking; Grant ID: 735160), which is gratefully acknowledged.

Conflicts of Interest: The authors declare no conflict of interest.

Appendix A

The theory of the distribution of relaxation times is briefly outlined here. The impedance can be shown with an equation consisting of an integral with time constants between 0 and ∞ and the distribution function $\gamma(\tau)$:

$$\underline{Z}(\omega) = R_0 + R_{\text{pol}} \int_0^\infty \frac{\gamma(\tau)}{1 + j\omega\tau} \mathrm{d}\tau \tag{A1}$$

with

$$\int_0^\infty \gamma(\tau)\mathrm{d}\tau = 1 \tag{A2}$$

where j is the imaginary unit and $\omega = 2\pi f$ is the angular frequency. Equation (A1) demonstrates an impedance spectrum containing an ohmic resistance R_0 and an overall polarization resistance R_{pol}. It is noteworthy that this representation model does not carry a specific physical meaning but solely represents the observed impedance spectrum's system dynamics [41].

An approximate estimation of $\gamma(\tau)$ (a continuous function) can be calculated by the γ_n (discrete function) for a finite number of serial resistor capacitor (RC) elements with logarithmically distributed τ_n values:

$$\underline{Z}(\omega) = R_0 + R_{\text{pol}} \sum_{n=1}^{N} \frac{\gamma_n}{1 + j\omega\tau_n} \tag{A3}$$

where γ_n weighs the proportion of the n-th RC element to the total polarization resistance (with the relaxation time n). [28]. The computation of γ_n is an inverse ill-posed problem, and inverse problems can be numerically approximated with regularization. [42]. The advantages of the DRT method are illustrated in Figure 1, where the imaginary part of the impedance spectrum is compared to the distribution function. In contrast to the imaginary region of the complex impedance, in which different processes overlap, the DRT has six distinct peaks [40]. Each physical polarization process is represented by a peak [43]. The characteristic relaxation frequency of each polarization process in the DRT may be precisely determined using the associated peak frequency [17]. The area specific resistance (ASR) of the underlying physicochemical process is represented by the area contained by each peak [44]. In addition, peak height and half-width relative to peak height provide qualitative information about the underlying physical process's time-constant dispersion [45].

Appendix B

The procedure of identifying the physicochemical processes using the DRT spectra via the variation of operating conditions is outlined here.

Appendix B.1. Temperature Variation

By analyzing Figure A1, it is possible to observe the trends of the DRT functions at different temperatures (650/675/700 °C). All the previously described processes (P1 to P5)

can be identified in the DRT plots, with different amplitudes and contributions according to the analyzed sample. The DRT amplitude is generally higher for T = 650 °C, with respect to other temperatures, due to increased resistance of the cell at lower temperatures.

By observing the variation in the DRT spectra with temperature, it is possible to observe temperature-related dependencies, which are typically related to charge transfer mechanisms. The two high-frequency processes, P1 and P2, are barely affected by a change in the anodic composition but are influenced by a temperature variation. This behavior suggests a fast, thermally activated process underlying these peaks; thus, they can be ascribed to the charge transfer mechanism related to the hydrogen electrochemical oxidation occurring at the anode functional layer, together with the oxygen ion transport within the YSZ lattice. Additionally, peak P3 appears to be unaffected by the modification of anodic molar fractions but shows a dependency on the operating temperature, which allows us to associate this feature with the charge transfer mechanism related to the oxygen reduction within the cathode layer.

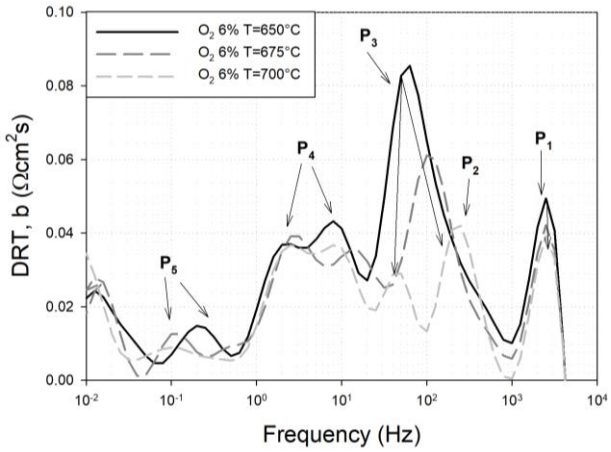

Figure A1. Effect of temperature variation on the DRT spectra.

Appendix B.2. Hydrogen Partial Pressure Variation

Secondly, the effect of hydrogen changes on the DRT shift is investigated. When the anodic composition and operating temperature are altered, two separate characteristics, one around 1 Hz and the other around 10 Hz, show highly comparable behavior in the lower-frequency zone: they both show a prominent dependency on the anodic molar fraction variations, while the increase in the temperature only marginally influences them. Therefore, it is reasonable to ascribe these two peaks to a single mass transport phenomenon (P4) associated with the diffusion of gas species through the porosity of the anode supporting layer of the cell. Mass transport phenomena are frequently represented by a distributed circuit element, known as the Warburg element in the EIS field. The DRT function calculated for a Warburg impedance response results in a principal peak, falling at the characteristic frequency of the process, followed by a set of satellite peaks, with decreasing intensity, at higher frequencies, which is also observed in the analyzed DRT spectra. This also confirms the validity of pre-allocating six frequency bandwidths with seven DRT peaks (with peak P4 and P4' within the same frequency bandwidth, related to mass transport) in the preliminary frequency bandwidth input required by the tool.

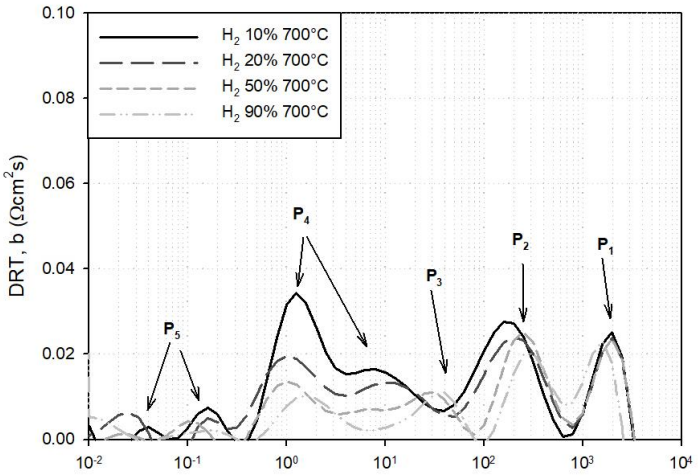

Figure A2. Effect of hydrogen variation on the DRT spectra.

Appendix B.3. Oxygen Partial Pressure Variation

Finally, the impact of oxygen partial pressure is analyzed, which mainly affects the cathode processes. A first effect related to oxygen content is observed at high frequency (around 100 Hz), attributed to the cathode charge transfer mechanisms P3. Due to the overlapping of the cathodic process P3 with the anodic process P2, it is hard to evaluate the effect of the oxygen variation on this process. Nevertheless, a reduction in its intensity is still noticeable. The process P5 falling at a very low frequency (<0.1 Hz) is only slightly affected by the variation in oxygen content and does not change with a change in the anode composition and temperature: it can be hypothesized to be the contribution of the gas diffusion through the porosity of the cathode layer. However, due to the low-frequency range, the signal quality is relatively low (measurement noise and scattering); thus, no significant trends of P5 with oxygen content can be clearly defined.

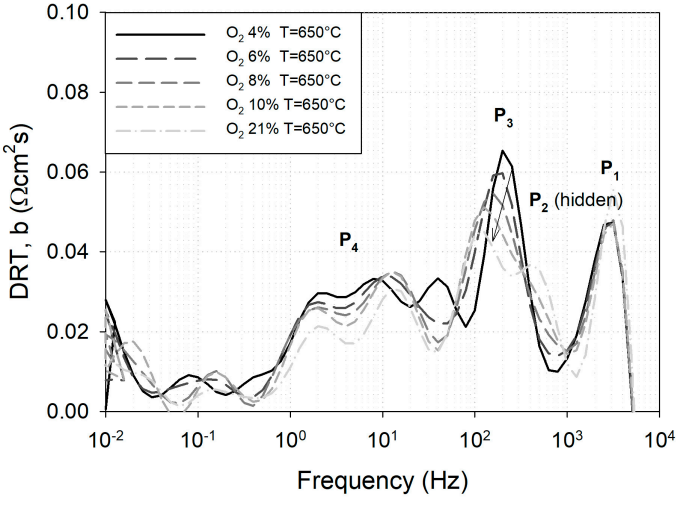

Figure A3. Effect of oxygen variation on the DRT spectra.

References

1. Buffo, G.; Ferrero, D.; Santarelli, M.; Lanzini, A. Energy and Environmental Analysis of a Flexible Power-to-X Plant Based on Reversible Solid Oxide Cells (RSOCs) for an Urban District. *J. Energy Storage* **2020**, *29*, 101314. [CrossRef]
2. Choudhury, A.; Chandra, H.; Arora, A. Application of Solid Oxide Fuel Cell Technology for Power Generation—A Review. *Renew. Sustain. Energy Rev.* **2013**, *20*, 430–442. [CrossRef]
3. Elmer, T.; Worall, M.; Wu, S.; Riffat, S.B. Emission and Economic Performance Assessment of a Solid Oxide Fuel Cell Micro-Combined Heat and Power System in a Domestic Building. *Appl. Therm. Eng.* **2015**, *90*, 1082–1089. [CrossRef]

4. Zhu, W.; Ding, D.; Xia, C. Enhancement in Three-Phase Boundary of SOFC Electrodes by an Ion Impregnation Method: A Modeling Comparison. *Electrochem. Solid-State Lett.* **2008**, *11*, 5009. [CrossRef]
5. Dubois, A.; Ricote, S.; Braun, R.J. Benchmarking the Expected Stack Manufacturing Cost of next Generation, Intermediate-Temperature Protonic Ceramic Fuel Cells with Solid Oxide Fuel Cell Technology. *J. Power Sources* **2017**, *369*, 65–77. [CrossRef]
6. Del Zotto, L.; Ferrario, A.M.; Hatunoglu, A.; Dell'era, A.; Mcphail, S.; Bocci, E. Experimental Procedures & First Results of an Innovative Solid Oxide Fuel Cell Test Rig: Parametric Analysis and Stability Test. *Energies* **2021**, *8*, 2038. [CrossRef]
7. De Haart, L.G.J.; Mougin, J.; Posdziech, O.; Kiviaho, J.; Menzler, N.H. Stack Degradation in Dependence of Operation Parameters; the Real-SOFC Sensitivity Analysis. *Fuel Cells* **2009**, *9*, 794–804. [CrossRef]
8. Arsalis, A. A Comprehensive Review of Fuel Cell-Based Micro-Combined-Heat-and-Power Systems. *Renew. Sustain. Energy Rev.* **2019**, *105*, 391–414. [CrossRef]
9. Mehr, A.S.; Lanzini, A.; Santarelli, M.; Rosen, M.A. Polygeneration Systems Based on High Temperature Fuel Cell (MCFC and SOFC) Technology: System Design, Fuel Types, Modeling and Analysis Approaches. *Energy* **2021**, *228*, 120613. [CrossRef]
10. Ma, S.; Loreti, G.; Wang, L.; Maréchal, F.; van herle, J.; Dong, C. Comparison and Optimization of Different Fuel Processing Options for Biogas-Fed Solid-Oxide Fuel Cell Plants. *Int. J. Hydrogen Energy* **2022**, *47*, 551–564. [CrossRef]
11. Hussain, S.; Yangping, L. Review of Solid Oxide Fuel Cell Materials: Cathode, Anode, and Electrolyte. *Energy Transit.* **2020**, *4*, 113–126. [CrossRef]
12. Thambiraj, N.; Suciu, C.; Waernhus, I.; Vik, A.; Hoffmann, A.C. Effect of Oxygen Depletion to the Cathode on the Working of Solid Oxide Fuel Cells. *ECS Trans.* **2017**, *78*, 875–887. [CrossRef]
13. Beale, S.B.; Andersson, M.; Boigues-Muñoz, C.; Frandsen, H.L.; Lin, Z.; McPhail, S.J.; Ni, M.; Sundén, B.; Weber, A.; Weber, A.Z. Continuum Scale Modelling and Complementary Experimentation of Solid Oxide Cells. *Prog. Energy Combust. Sci.* **2021**, *85*, 100902. [CrossRef]
14. Lasia, A. Electrochemical Impedance Spectroscopy and Its Applications. In *Modern Aspects of Electrochemistry*; Kluwer Academic Publishers: Amsterdam, The Netherlands, 2005; pp. 143–248.
15. Nechache, A.; Mansuy, A.; Petitjean, M.; Mougin, J.; Mauvy, F.; Boukamp, B.A.; Cassir, M.; Ringuedé, A. Diagnosis of a Cathode-Supported Solid Oxide Electrolysis Cell by Electrochemical Impedance Spectroscopy. *Electrochim. Acta* **2016**, *210*, 596–605. [CrossRef]
16. Boukamp, B.A. Electrochemical Impedance Spectroscopy in Solid State Ionics: Recent Advances. *Solid State Ion.* **2004**, *169*, 65–73. [CrossRef]
17. Li, X.; Ahmadi, M.; Collins, L.; Kalinin, S.V. Deconvolving Distribution of Relaxation Times, Resistances and Inductance from Electrochemical Impedance Spectroscopy via Statistical Model Selection: Exploiting Structural-Sparsity Regularization and Data-Driven Parameter Tuning. *Electrochim. Acta* **2019**, *313*, 570–583. [CrossRef]
18. Boukamp, B.A.; Rolle, A. Use of a Distribution Function of Relaxation Times (DFRT) in Impedance Analysis of SOFC Electrodes. *Solid State Ion.* **2018**, *314*, 103–111. [CrossRef]
19. Zhang, Y.; Chen, Y.; Li, M.; Yan, M.; Ni, M.; Xia, C. A High-Precision Approach to Reconstruct Distribution of Relaxation Times from Electrochemical Impedance Spectroscopy. *J. Power Sources* **2016**, *308*, 1–6. [CrossRef]
20. Sumi, H.; Shimada, H.; Yamaguchi, Y.; Yamaguchi, T.; Fujishiro, Y. Degradation Evaluation by Distribution of Relaxation Times Analysis for Microtubular Solid Oxide Fuel Cells. *Electrochim. Acta* **2020**, *339*, 135913. [CrossRef]
21. Sonn, V.; Leonide, A.; Ivers-Tiffée, E. Combined Deconvolution and CNLS Fitting Approach Applied on the Impedance Response of Technical Ni/8YSZ Cermet Electrodes. *J. Electrochem. Soc.* **2008**, *155*, B675. [CrossRef]
22. Žnidarič, L.; Nusev, G.; Morel, B.; Mougin, J.; Juričić, Đ.; Boškoski, P. Evaluating Uncertainties in Electrochemical Impedance Spectra of Solid Oxide Fuel Cells. *Appl. Energy* **2021**, *298*, 117101. [CrossRef]
23. Leonide, A.; Sonn, V.; Weber, A.; Ivers-Tiffée, E. Evaluation and Modeling of the Cell Resistance in Anode-Supported Solid Oxide Fuel Cells. *J. Electrochem. Soc.* **2008**, *155*, B36. [CrossRef]
24. Xia, J.; Wang, C.; Wang, X.; Bi, L.; Zhang, Y. A Perspective on DRT Applications for the Analysis of Solid Oxide Cell Electrodes. *Electrochim. Acta* **2020**, *349*, 136328. [CrossRef]
25. Pumiglia, D.; Massimiliano, D.P.; Monforti Ferrario, A.; McPhail, S.; Pylypko, S. Impedance-Based Solid Oxide Fuel Cell Testing as Scalable and Reliable Quality Control Tool for Cell and Batch Manufacturing: First Findings. *E3S Web Conf.* **2022**, *334*, 04021. [CrossRef]
26. Osinkin, D.A. An Approach to the Analysis of the Impedance Spectra of Solid Oxide Fuel Cell Using the DRT Technique. *Electrochim. Acta* **2021**, *372*, 137858. [CrossRef]
27. Gallo, M.; Polverino, P.; Mougin, J.; Morel, B.; Pianese, C. Coupling Electrochemical Impedance Spectroscopy and Model-Based Aging Estimation for Solid Oxide Fuel Cell Stacks Lifetime Prediction. *Appl. Energy* **2020**, *279*, 115718. [CrossRef]
28. Wan, T.H.; Saccoccio, M.; Chen, C.; Ciucci, F. Influence of the Discretization Methods on the Distribution of Relaxation Times Deconvolution: Implementing Radial Basis Functions with DRTtools. *Electrochim. Acta* **2015**, *184*, 483–499. [CrossRef]
29. Risse, S.; Cañas, N.A.; Wagner, N.; Härk, E.; Ballauff, M.; Friedrich, K.A. Correlation of Capacity Fading Processes and Electrochemical Impedance Spectra in Lithium/Sulfur Cells. *J. Power Sources* **2016**, *323*, 107–114. [CrossRef]
30. Žic, M.; Pereverzyev, S.; Subotić, V.; Pereverzyev, S. Adaptive Multi-Parameter Regularization Approach to Construct the Distribution Function of Relaxation Times. *GEM-Int. J. Geomath.* **2020**, *11*, 1382. [CrossRef]

31. Kulikovsky, A. PEM Fuel Cell Distribution of Relaxation Times: A Method for the Calculation and Behavior of an Oxygen Transport Peak. *Phys. Chem. Chem. Phys.* **2020**, *22*, 19131–19138. [CrossRef]
32. KOBAYASHI, K.; SUZUKI, T.S. Extended Distribution of Relaxation Time Analysis for Electrochemical Impedance Spectroscopy. *Electrochemistry* **2022**, *90*, 21-00111. [CrossRef]
33. Boigues Muñoz, C.; Pumiglia, D.; McPhail, S.J.; Montinaro, D.; Comodi, G.; Santori, G.; Carlini, M.; Polonara, F. More Accurate Macro-Models of Solid Oxide Fuel Cells through Electrochemical and Microstructural Parameter Estimation—Part I: Experimentation. *J. Power Sources* **2015**, *294*, 658–668. [CrossRef]
34. Boigues-Muñoz, C.; Pumiglia, D.; McPhail, S.J.; Santori, G.; Montinaro, D.; Comodi, G.; Carlini, M.; Polonara, F. More Accurate Macro-Models of Solid Oxide Fuel Cells through Electrochemical and Microstructural Parameter Estimation—Part II: Parameter Estimation. *J. Power Sources* **2015**, *286*, 321–329. [CrossRef]
35. Silva-Mosqueda, D.M.; Elizalde-Blancas, F.; Pumiglia, D.; Santoni, F.; Boigues-Muñoz, C.; McPhail, S.J. Intermediate Temperature Solid Oxide Fuel Cell under Internal Reforming: Critical Operating Conditions, Associated Problems and Their Impact on the Performance. *Appl. Energy* **2019**, *235*, 625–640. [CrossRef]
36. Zhu, H.; Kromp, A.; Leonide, A.; Ivers-Tiffée, E.; Deutschmann, O.; Kee, R.J. A Model-Based Interpretation of the Influence of Anode Surface Chemistry on Solid Oxide Fuel Cell Electrochemical Impedance Spectra. *J. Electrochem. Soc.* **2012**, *159*, F255–F266. [CrossRef]
37. Kromp, A.; Dierickx, S.; Leonide, A.; Weber, A.; Ivers-Tiffée, E. Electrochemical Analysis of Sulfur-Poisoning in Anode Supported SOFCs Fuelled with a Model Reformate. *J. Electrochem. Soc.* **2012**, *159*, B597–B601. [CrossRef]
38. Wuillemin, Z.; Antonetti, Y.; Beetschen, C.; Millioud, O.; Ceschini, S.; Madi, H.; van herle, J. Local Activation and Degradation of Electrochemical Processes in a SOFC. *ECS Trans.* **2013**, *57*, 561–570. [CrossRef]
39. Endler, C.; Leonide, A.; Weber, A.; Tietz, F.; Ivers-Tiffée, E. Time-Dependent Electrode Performance Changes in Intermediate Temperature Solid Oxide Fuel Cells. *J. Electrochem. Soc.* **2010**, *157*, B292. [CrossRef]
40. Dierickx, S.; Weber, A.; Ivers-Tiffée, E. How the Distribution of Relaxation Times Enhances Complex Equivalent Circuit Models for Fuel Cells. *Electrochim. Acta* **2020**, *355*, 136764. [CrossRef]
41. Ciucci, F.; Chen, C. Analysis of Electrochemical Impedance Spectroscopy Data Using the Distribution of Relaxation Times: A Bayesian and Hierarchical Bayesian Approach. *Electrochim. Acta* **2015**, *167*, 439–454. [CrossRef]
42. Dion, F.; Lasia, A. The Use of Regularization Methods in the Deconvolution of Underlying Distributions in Electrochemical Processes. *J. Electroanal. Chem.* **1999**, *475*, 28–37. [CrossRef]
43. Effat, M.B.; Ciucci, F. Bayesian and Hierarchical Bayesian Based Regularization for Deconvolving the Distribution of Relaxation Times from Electrochemical Impedance Spectroscopy Data. *Electrochim. Acta* **2017**, *247*, 1117–1129. [CrossRef]
44. Malkow, K.T. A Theory of Distribution Functions of Relaxation Times for the Deconvolution of Immittance Data. *J. Electroanal. Chem.* **2019**, *838*, 221–231. [CrossRef]
45. Boukamp, B.A.; Rolle, A. Analysis and Application of Distribution of Relaxation Times in Solid State Ionics. *Solid State Ion.* **2017**, *302*, 12–18. [CrossRef]